Laminar Separation Bubble Noise in a Propeller Operating at Low-Reynolds Numbers

Edoardo Grande[1], Daniele Ragni[1], Francesco avallone[1] and Damiano Casalino[1]

[1]Department of Flight, University of Science
Delft University of Technology, Delft, 2629HS, The Netherlands

Abstract

This paper focuses on how a laminar separation bubble (LSB) contributes to noise generation on a propeller operating at low-Reynolds number. Microphone measurements of a propeller with both clean and forced boundary layer transition blades are carried out in the A-Tunnel at TU Delft by varying the propeller advance ratio J from 0 to 0.6, corresponding to a tip Reynolds number ranging from $4.3 \cdot 10^4$ to 10^5. The flow behaviour on the blade surface and around the propeller is studied via oil-flow visualizations and particle image velocimetry (PIV). At J = 0.4 and 0.6, vortex shedding from the LSB causes high-frequency noise which appears as a hump in the far-field noise spectra. Forcing the location of the boundary layer transition suppresses the LSB and, consequently, the hump, reducing the noise emission of about 5 and 10 dB at J = 0.4 and 0.6, respectively. Vortex shedding noise is further modeled by using a semi-empirical method.

1 Introduction

Low-Reynolds numbers flows over rotating blades are of great interest for the design of several devices, such as unmanned aerial vehicles, micro aerial vehicles and urban wind turbines. These devices usually employ small-scale rotors, which operate at a chord Reynolds number Re_c ranging from 10^4 to 10^5. At such low-Reynolds numbers, the boundary layer on the propeller blades is usually subjected to a laminar separation, even at low angles of attack. The separated shear layer gains momentum from the free-stream and reattaches as turbulent boundary layer, forming a laminar separation bubble (LSB) [18]. The formation of the LSB influences the aerodynamic performances and can be responsible of noise radiation.

Grande et al. [7] and Leslie et al. [10] shed light on the different noise sources which are simultaneously present in a small-scale propeller . In particular, they showed that, for some operating conditions, the vortex shedding generated from a LSB constitutes the predominant noise source at high-frequency and is responsible for a hump in the far-field noise spectra. However, the research on these kind of propellers is limited by several numerical and experimental challenges. On the numerical side, the main challenges are related to the capability of the CFD solver to correctly predict the transitional flow behaviour [15]. On the experimental side instead, flow velocimetry on the blades are made difficult due to the small chordwise dimensions of the blades and to fact that the system is rotating. Furthermore, acoustic measurements are contaminated by electrical motor noise [9, 8] and vibrations of the test-rig.

The studies focusing on steady airfoils reveal that, as the angle of attack (or Reynolds number) increases, the LSB moves upstream and decreases in length [4]. The decrease in length of the LSB as the angle of attack increases continue until the the separation and reattachment point occur at the same point (in the vicinity of the leading edge) and the bubble bursts. In this case a laminar separationn is still present but the separated shear layer is not able to reattach anymore. This causes a pronounced decrease in lift and increase in drag. At very low Reynolds numbers, a LSB can burst at low angles of attack and the lift polar shows a substantial decrease of the curve slope due to a lower suction peak (with respect to the corresponding inviscid case), as shown by Yarusevich at al. [19] and by Abathi and Marchman [11].

A laminar separation bubble located sufficiently close to the airfoil trailing edge is responsible of tonal noise emission [14]. Indeed, coherent vortices, result of amplified instability (Tollmien-Schlichting) waves into the laminar boundary layer, roll-up over the separated shear layer and produces tonal noise during their passage over

the trailing edge. The coherence of the vortical structures at the trailing edge is a necessary condition for tonal noise emission. The acoustic pressure waves scattered at the trailing edge propagate upstream and trigger the generation of new instability waves. Hence, a so-called "feedback loop" is created between the trailing edge and the upstream point where the hydrodynamic instabilities are formed. It is not clear whether the presence of a feedback loop is a necessary condition for the tonal noise generation and there is no agreement on the physics and exact chordwise position of the feedback loop [2].

Arbey and Bataille [1] found that the spectrum of the radiated noise from NACA airfoils consists of a broadband hump, centered at a frequency f_s, and a dominant (or central) tone, at a frequency $f_{n_{MAX}}$, surrounded by a series of regularly spaced tones at frequencies f_n. Paterson et al. [13] observed that the main tone frequency exhibits a so-called "ladder-structure", i.e., for a small range of free-stream velocities U_∞, it increases as $U_\infty^{0.8}$ and, at certain velocities, it jumps to higher frequencies following a new $U_\infty^{0.8}$ power relationship with the velocity. Globally, the average trend of the main tone frequency (obtained by fitting a straight line through all the data points) follows a 3/2 power of the free-stream velocity, hence $f_{n_{MAX}} \propto U_\infty^{1.5}$. While Paterson's model estimates only the vortex shedding tone frequency, the only available model that predicts the amplitude of the tones is the airfoil self noise model from Brooks et al. [5] (in the following referred as BPM model). The latter is a semi-empirical model based on a wind tunnel data set on NACA 0012 airfoils of different sizes.

It is not known if the current knowledge about noise generation due to laminar vortex shedding from steady airfoils applies also to rotating blades. In this case, the spanwise variation of velocity and angle of attack can influence the formation of the LSB and the coherence of the shed vortices. The aim of this work is to study the characteristics of the LSB for a propeller operating at low-Reynolds numbers and to explain how the LSB contributes to a significant noise emission. To this purpose, the propeller is tested at a tip Reynolds number between $4.3 \cdot 10^4$ and 10^5. A combination of far-field noise measurements, phase-locked stereoscopic PIV and oil-flow visualization are used to quantify the noise radiation and to visualize the flow around the propeller and on the blade surface, respectively. A comparison is presented for the case of the propeller with smooth surface and with a turbulator applied on both the suction and pressure side to force the transition of the boundary layer from laminar to turbulent. A physical interpretation of the acoustic spectra is given by extending the BPM model to rotating blades.

The abstract is organized as follows. In Sec. 2 the propeller geometry is presented together with the experimental setup. In Sec. 3 the aerodynamic and aeroacoustic results are discussed. Finally, the main conclusions of the work are summarized in Sec. 4.

2 Propeller geometry and experimental setup

The propeller used for this research is inspired from an APC 9x6. It is a two-bladed propeller, constituted of NACA 4412 airfoil sections, with a diameter $D = 30$ cm. Measurements are conducted both with a smooth blades surface (denoted as clean) and with a turbulator applied on both pressure and suction side of the propeller blades (denoted as forced-BL). The turbulator fixes the boundary layer transition location and it is realized as a flat strip with a thickness of 0.05 mm and a chordwise length of 1 mm and it is applied at 25% of the chord. The propeller is tested in the anechoic tunnel (A-tunnel) of TU Delft. The A-tunnel is a vertical, open-jet wind tunnel and the exit nozzle employed is circular, with an exit diameter of 0.60 m and a contraction ratio of 15:1. A more detailed description of the propeller geometry and test-rig can be found in Grande et al. [7], while the A-tunnel details of the flow and acoustics characterization, can be found in Merino-Martinez et al. [12].

The propeller is operated at three rotational velocities, 4000, 5000 and 6000 rpm, over a range of advance ratios $J = V_\infty/nD$ between 0 and 0.6 (where V_∞ is the axial flow speed in m/s, n is the propeller rotational frequency in Hz and D is the propeller diameter in m). The tip Reynolds number is varied from $4.3 \cdot 10^4$ to 10^5.

2.1 Acoustic measurements

The acoustic measurements are performed by means of a linear microphone array, constituted by 13 G.R.A.S. 40PH analog free field microphones, having a diameter of 7 mm, a frequency range between 10 Hz and 20 KHz and a maximum SPL of 135 dB. As shown in Fig. 1, the microphone array is perpendicular to the propeller plane and located at a distance of 4D (1.2 m) from the propeller axis. The distance between each microphone is 0.5D (0.15 m), the microphone 7 is aligned with the propeller plane, the microphone 1 is 3D (0.9 m) above the propeller plane and the microphone 13 is 3D below. The microphones have been calibrated using a G.R.A.S. 42AA pistonphone with a calibration level of 114 dB re. 20 μPa. The uncertainty of the calibration is less than 0.09 dB (99% confidence level). The data acquisition system consists of a National Instrument PXIe-4499 sound and

vibrations data acquisition module. Microphone voltages have been recorded for a duration of 30 s at a frequency rate of 50 KHz. The acoustic signals are separated in 300 Welch blocks with 50% overlap, corresponding to a bandwidth of 10 Hz.

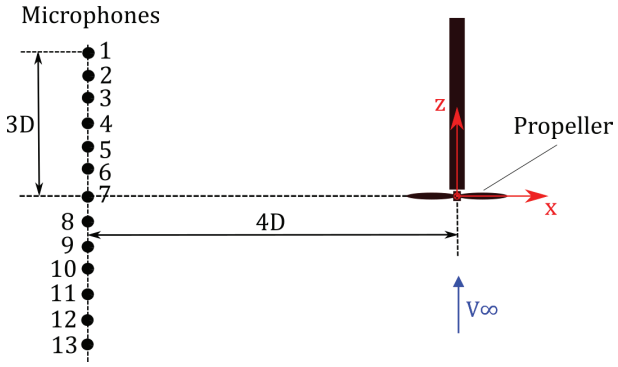

Figure 1: Microphone array configuration.

2.2 PIV measurements

Stereoscopic PIV measurements are conducted to study the flow over the cross section of the blade at r/R = 60% and in the propeller wake. The flow is seeded with particles lower than 1 micrometer median diameter produced by a SAFEX Twin Fog generator with SAFEX-Inside-Nebelfluid, a mixture of dyethelene glycol and water. Illumination is provided by a double cavity Quantel Evergreen EVG00200 Nd:YAG laser with 200 mJ/pulse energy. Figure 2 shows the laser and camera configuration adopted for both the type of measurements. A total of four Imager sCMOS camera (2560 x 2160 px), two for the suction side and two for the pressure side, equipped with Scheimpflug adapters and four Nikon lenses with 200 mm focal length at f# 11 are used for the cross section measurements, whereas two imager sCMOS camera equipped with Scheimpflug adapters and two Nikon lenses with 60 mm focal length at f# 8 for the wake measurements. The camera calibration, acquisition and post-processing have been carried out with the LaVision Davis 8.4 software.

To measure the flow over the cross-section of the blade, avoiding shadow region in the field of view, two laser sheets of about 1 mm of thickness are created, one illuminating the suction side of the cross-section and one the pressure side (see Fig. 2a). Hence, the final field of view is the combination of two fields of view. To converge statistics, sets of 500 images are recorded in phase-locked mode. To obtain phase-locked measurements a trigger signal from the encoder mounted on the motor shaft is used to control the timing of laser and camera. For the cross section measurements, the images are acquired when the propeller section is aligned with the laser plane, as depicted in Fig. 2a (bottom). For the wake measurements instead, three propeller phases are chosen, i.e. $\phi = 0°$, $\phi = 45°$, $\phi = 90°$ (see. Fig 2b).

The images are processed with a cross-correlation algorithm employing the window deformation iterative multi-grid [16] with final interrogation window size of 24 x 24 pixels and 75% overlap for the sectional measurements and 16 x 16 pixels and 75% overlap for the wake measurements. Spurious vectors are identified through a median filter and replaced by interpolation. Details of the PIV setup apparatus are collected in Table 1.

Table 1: Details of PIV setup for the cross section (a) and wake (b) measurements.

Imaging parameters	Wake measurements	Cross section measurements
Camera	2 Imager sCMOS	4 Imager sCMOS
Number of pixels [px]	2560 x 2160	2560 x 2160
Pixel size [μm]	6.5 x 6.5	6.5 x 6.5
Focal length [mm]	60	200
Magnification	0.1	0.37
Imaging resolution [px/mm]	$\approx$ 15	$\approx$56
FOV [cm^2]	16 x 16	4.5 x 4
Spatial resolution [mm]	$\approx$ 0.28	$\approx$ 0.4
f#	8	11

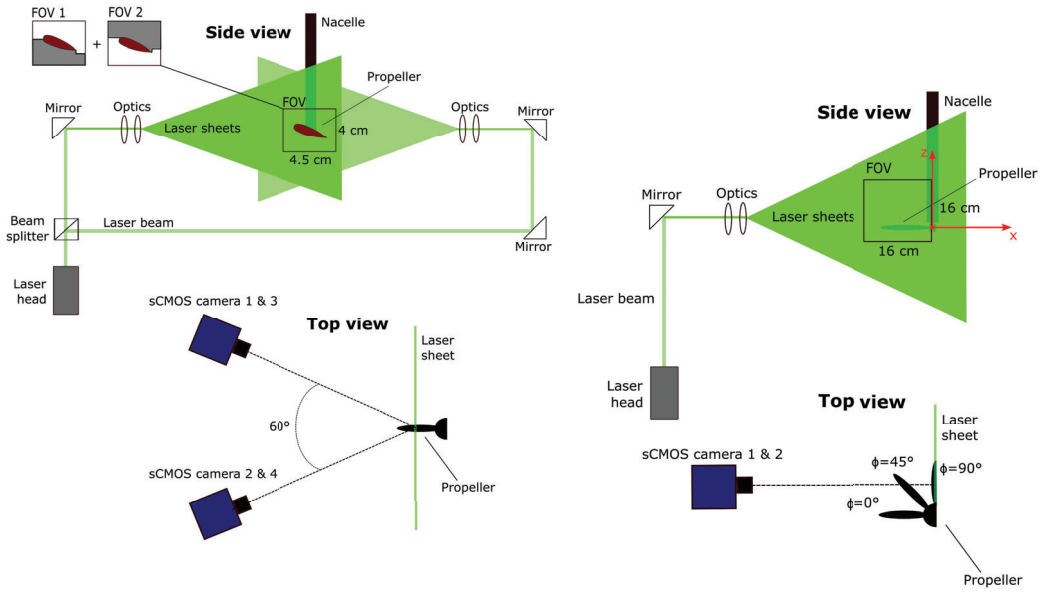

(a) (b)

Figure 2: Sketch of PIV laser and camera configurations for the cross section (a) and wake (b) measurements.

2.3 Oil-flow visualizations

To visualize the surface flow pattern on the propeller blade, surface oil-flow visualizations are carried out. A mixture obtained from 50 mL liquid-paraffin wax and 15-25 drops of fluorescent oil additive A-680 is used. The oil-flow tests are conducted as follows. A film of oil is applied on the blade surface. The propeller is brought to the required operating conditions and is run for about 8-10 min to let the mixture to properly establish on the blade surface. Finally, the propeller is slowly stopped, then it is illuminated at rest with an ultraviolet lamp with a wide aperture and pictures of the blade surface are taken.

3 Results

3.1 Oil-flow visualizations

Figure 3 shows the oil-flow visualizations of the suction side of the propeller blade for both the clean and forced-BL cases at 4000 rpm and J varying from 0 to 0.6. For all the cases, the blade portions where the oil accumulates (green area marked with S) represents regions with flow separation. These regions are characterized by a chordwise pressure gradient that is almost zero and, as a consequence, the flow is predominantly radial.

The clean case (Fig. 3 up) reveals a presence of a LSB at J between 0 and 0.4. The LSB is represented by the green region enclosed between the separation and reattachment lines, highlighted with dashed magenta and red lines, respectively. The LSB length increases with J, because of a decrease of the local angle of attack along the blade. Unlike the other cases, at $J = 0$ the LSB does not extend up to the tip and this is ascribed to the tip vortex, that washes out the LSB at the tip region [17, 3]. For the case $J = 0.6$, the flow separates but it is not very clear if it reattaches in proximity of the trailing edge. Thus, a bubble bursting might occur.

When the turbulator is used (Fig. 3 down), the LSB is suppressed and all the cases exhibit a similar behaviour. After the turbulator line the flow is attached and eventually separates close to the trailing edge. The separated region extends up to the tip only at $J = 0$ and reduces in size as the advance ratio increases. This is probably due to the global decrease of the angle of attack over the entire blade as J increases.

3.2 Vorticity field around the cross-section at $\mathrm{r/R} = 0.6$

Figure 4 shows the instantaneous spanwise vorticity distribution (obtained with finite difference of order two from the PIV velocity fields) around the cross-section of the clean blade at $r/R = 0.6$ at 4000 rpm and J varying from

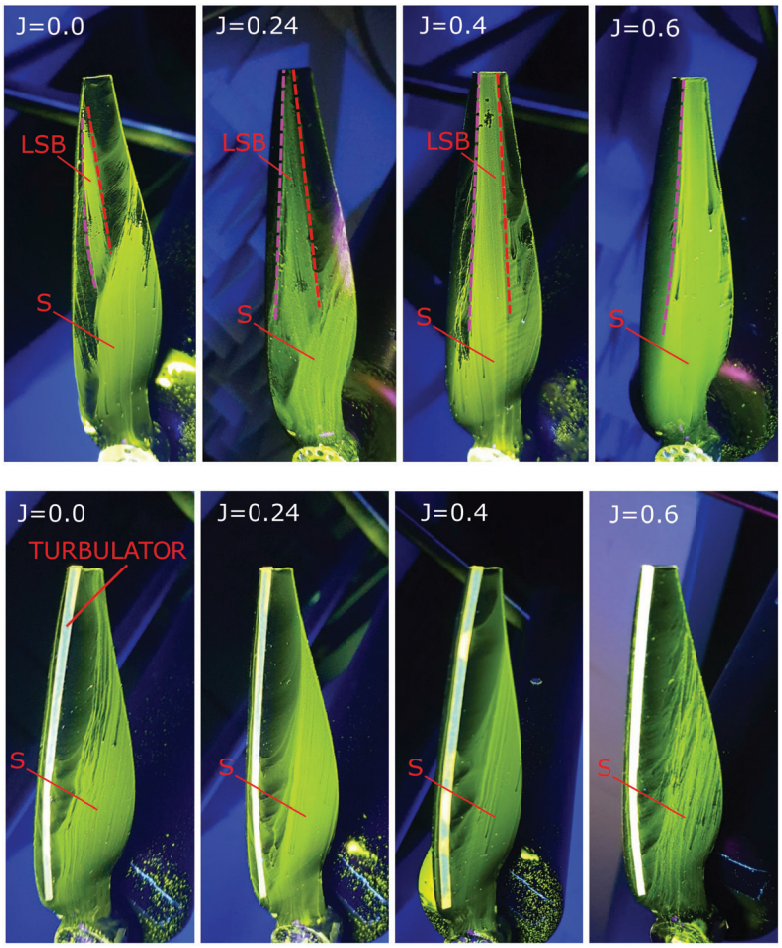

Figure 3: Oil flow visualizations of the suction side of the clean blade (up) and of the forced-BL blade (down) at 4000 rpm and **J** = 0, 0.24, 0.4 and 0.6.

0 to 0.6. The x and y axis are normalized with respect to the local airfoil chord and centered at the airfoil leading edge. Each vorticity field is combined with the corresponding oil-flow visualization of the blade suction side. The cross-section at r/R = 0.6 is marked with the horizontal magenta line.

The cases at J = 0.4 and 0.6 exhibit clear coherent vortex shedding in the near wake region (1 ¡ x/R ¡ 1.2), forming a vortex shedding. For the other two cases, i.e. J = 0 and 0.24, coherent structures in the near wake cannot be identified. Indeed, at low advance ratios the LSB has a smaller length and it is closer to the leading edge, as shown from the the oil-flow patterns in the left side of the figure. As a consequence, the vortex shedding is characterized by structures with a lower coherence and length scale, which might be not captured from the current PIV setup. The surface point on the suction side where the vorticity is non-zero (marked with O) moves toward the trailing edge as J increases, in agreement with the downstream displacement of the LSB. It is relevant to note that the length scale of the structures at J = 0.6 is larger compared with the case at J = 0.4. This strengthens the hypothesis of laminar separation without reattachment, mentioned in the previous section. In fact, as shown by Yarusevich [20], when the flow fails to reattach the scale of the wake structures is noticeably larger.

3.3 Experimental far-field noise spectra

Figure 5 shows the experimental far-field noise spectra (above $2 \cdot 10^3$ Hz) for the clean blade, computed by using the pressure signals from microphone 1. The spectra from the other microphones have the same trends and do not give additional information. Figure 5 (left) represents a comparison at a fixed rpm of 4000, by varying the J, Fig. 5 (right) represents instead a comparison at a fixed J of 0.6, by varying the rpm. In order to highlight the noise trends, a smoothing function that discard the tonal peaks due to the electric motor (as shown by Casalino et al. [6]), is applied to each spectrum and plotted on top of the real spectrum. The hump above $5 \cdot 10^3$ Hz, visible at

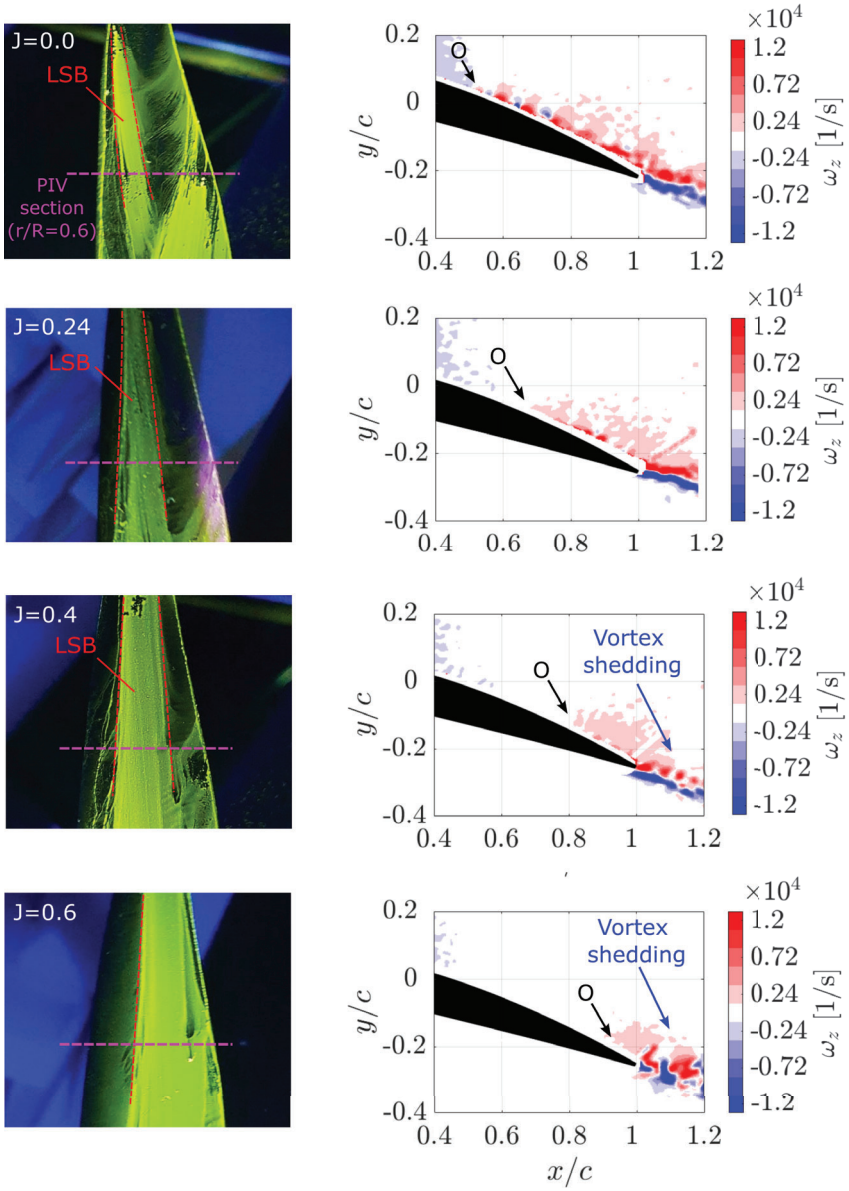

Figure 4: Instantaneous spanwise vorticity distribution (right) around the clean blade cross-section at $\mathbf{r/R}$ = 0.6 and oil-flow visualizations of the blade suction side at 4000 rpm. From top to bottom: $\mathbf{J}$ = 0, $\mathbf{J}$ = 0.24, $\mathbf{J}$ = 0.4 and $\mathbf{J}$ = 0.6.

$J = 0.4$ and $J = 0.6$, is due to the vortex shedding from the laminar separation bubble, as reported by Grande et al. [7]. A further indication is given by the Paterson' model, which predicts vortex shedding frequencies in the same frequency range. Indeed, since the chord and velocity vary along the blade, there is a range of frequencies (instead of a single tone) at which the vortex shedding noise is expected to be present. Overall, all the ranges are contained between $5 \cdot 10^3$ Hz and $4.7 \cdot 10^4$ Hz.

It is evident that the amplitude of the hump increases when J passes from 0.4 to 0.6. This is associated to the increase in length of the shed vortices (see Sec. 3.2) and, as a consequence, to a more efficient noise emission. For the cases J = 0 and 0.24, the lower coherence of the vortices at the trailing edge is expected to be responsible for the hump reduction. When the rpm is increased and J is kept equal to 0.6 (Fig. 5 right), the hump shifts toward higher frequencies and increases in amplitude. The frequency shifting is in agreement with the Paterson's model as it is dependent on the velocity ($f \propto U^{1.5}$). The increase in amplitude is due to the fact that, when the rpm increases (at a fixed J), the angle of attack over the blade decreases and, as explained above, this shifts the separated area over the trailing edge and make the vortex shedding noise more efficient.

Figure 6 shows the noise spectra for the forced-BL blade. As for the clean case, the left side represents a

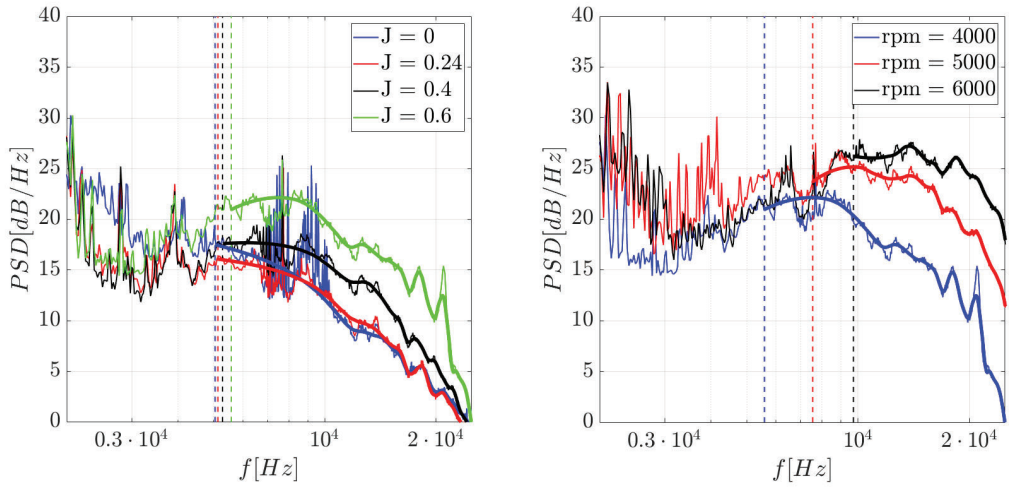

Figure 5: Comparison of noise spectra for the clean blade at a fixed rpm of 4000, by varying **J** (left) and a fixed J of 0.6, by varying the rpm (right).

comparison at a fixed rpm of 4000, by varying the J, instead the right side represents a comparison at a fixed J of 0.6, by varying the rpm. The turbulator suppresses the formation of the laminar separation bubble responsible for the hump. The main noise source for this case is expected to be turbulent boundary layer trailing edge noise. It is interesting to note that, when the rpm is kept constant and J increases, the spectra at high frequency collapse to the same level. This constitutes a further prove that the high frequency noise trend for the clean blade is strongly related to the LSB characteristics. On the other side, the increase of rpm at a fixed J of 0.6 causes an increase in the noise level. This is expected to be related to the increase with the velocity of the boundary layer integral parameters at the trailing edge.

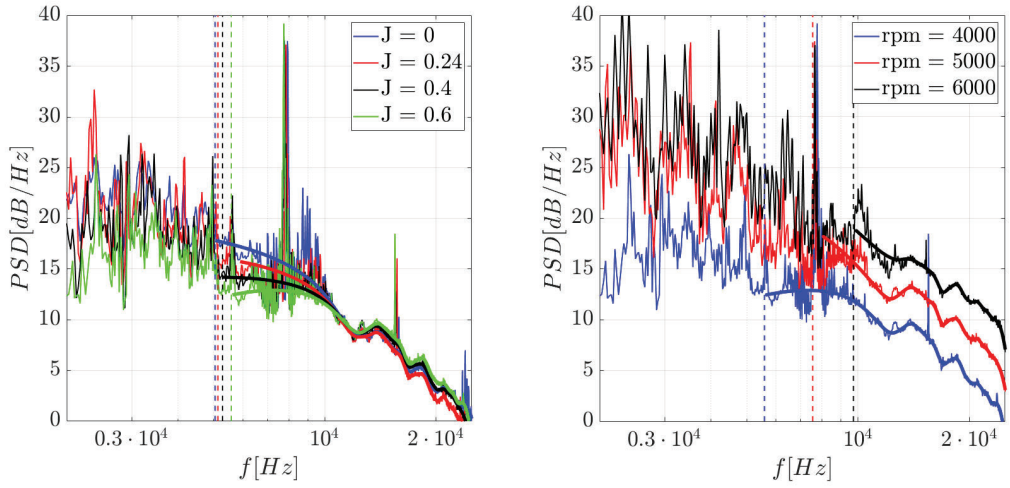

Figure 6: Comparison of noise spectra for the forced-BL blade at a fixed rpm of 4000, by varying **J** (left) and a fixed J of 0.6, by varying the rpm (right).

Figure 7 compares the noise spectra between the clean and forced-BL blade to easily infer the final conclusions about the LSB effect. At the lowest advance ratios, i.e. $J = 0$ (Fig. 7a) and 0.24 (Fig. 7b), the LSB, located close

to the blade leading edge, has almost no effect and the clean/forced-BL spectra coincide. At $J = 0.4$ (Fig. 7c) and 0.6 (Fig. 7d) the vortex shedding from the LSB, which has moved toward the blade trailing edge and increased in chordwise length, is the cause of an increment in noise level for the clean case of about 5 and 10 dB, respectively.

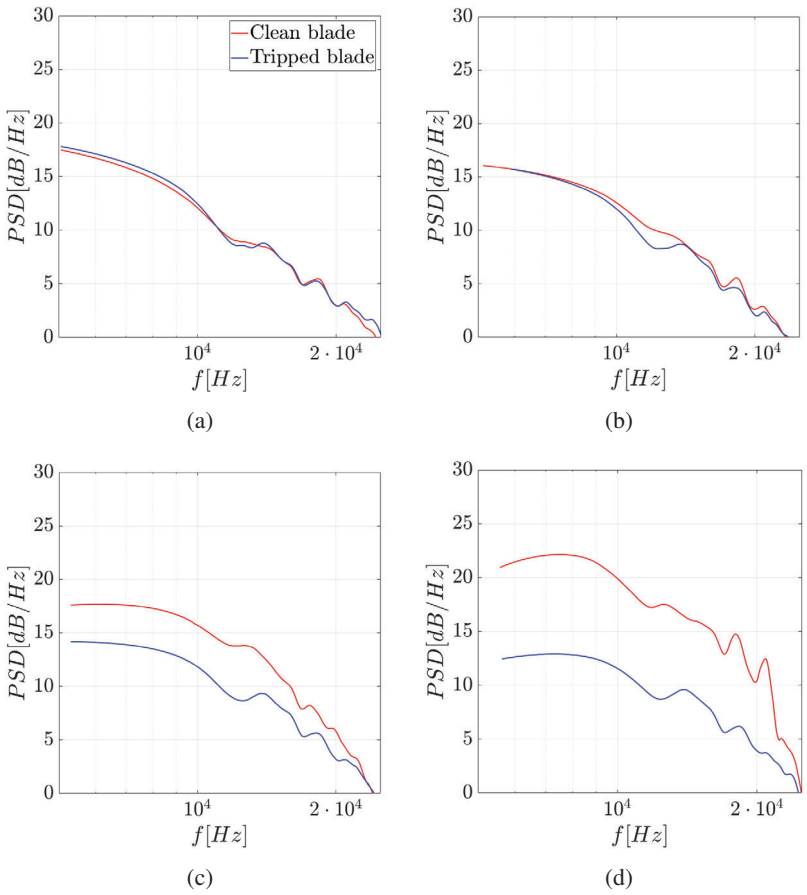

Figure 7: Comparison between clean and forced-BL noise spectra at 4000 rpm and $\mathbf{J = 0}$ (a), $\mathbf{J = 0.24}$ (b), $\mathbf{J = 0.4}$ (c), $\mathbf{J = 0.6}$ (d).

4 Conclusions

An investigation of the noise emitted by a laminar separation bubble on a small-scale propeller operating at low-Reynolds number was accomplished through experimental measurements in an anechoic wind tunnel. The propeller was tested both with a smooth surface (clean) and with a turbulator applied on both suction and pressure side of the blades to force the transition of the boundary layer from laminar to turbulent. Microphone measurements were complemented with oil-flow visualization of the blade surface and phase-locked PIV measurements of a blade cross-section and of the propeller slipstream. Physical insights of noise generation due to the LSB were retrieved by extending the semi-empirical BPM model [5] to rotating blades.

A laminar separation bubble was visualized on the suction side of the clean blade surface at $J = 0$, 0.24 and 0.4. At $J = 0.6$ the LSB probably bursts since there was not a visual evidence of flow reattachment. When the boundary layer transition location is forced, the LSB was suppressed and the flow appeared to be attached after the transition strip. The analysis of the instantaneous vorticity field around the cross-section at the 60% of the span revealed that the LSB is responsible for vortex shedding, characterized by coherent structures in the wake for the cases $J = 0.4$ and 0.6. The bigger length scale of the shed vortices at $J = 0.6$ was associated with the hypothesis of separation without reattachment. The shedding frequency, calculated by means of a statistical approach, was found to be 9635 Hz and 8600 Hz at $J = 0.4$ and 0.6, respectively. Vortical coherent structures were not clearly visible for the cases $J = 0$ and 0.24 and this was attributed to the loss of coherence due to the smaller chordwise length of the LSB and the closer vicinity of the latter to the blade leading edge.

The vortex shedding from the LSB is responsible for a high frequency hump in the far-field noise spectra at J = 0.4 and 0.6. In accordance with the Paterson's model, the hump shifts toward higher frequencies when the rpm is increased. The comparison between clean and forced-BL noise spectra showed that, when the turbulator is used, the hump was removed and the noise was reduced of about 5 dB at J = 0.4 and 10 dB at J = 0.6. This constitutes a further prove of the link between the LSB and high frequency noise radiation.

References

[1] H. Arbey and J. Bataille. Noise generated by airfoil profiles placed in a uniform laminar flow. *Journal of Fluid Mechanics*, 134:33–47, 1983.

[2] Elias Arcondoulis, Con Doolan, A Zander, and Laura Brooks. A review of trailing edge noise generated by airfoils at low to moderate reynolds number. *Acoustics Australia / Australian Acoustical Society*, 36, 03 2011.

[3] William G Bastedo Jr and Thomas J Mueller. Spanwise variation of laminar separation bubbles on wings at low reynolds number. *Journal of aircraft*, 23(9):687–694, 1986.

[4] Michael Boutilier and Serhiy Yarusevych. Parametric study of separation and transition characteristics over an airfoil at low reynolds numbers. *Experiments in Fluids*, 52, 06 2012.

[5] Thomas Brooks, Dennis Pope, and Michael Marcolini. Airfoil self-noise and prediction. *Nasa Reference Publication 1218*, 08 1989.

[6] D. Casalino, E. Grande, G. Romani, D. Ragni, and F. Avallone. Definition of a benchmark for low reynolds number propeller aeroacoustics. *Aeroaspace Science and Technology*, 2021.

[7] Edoardo Grande, Gianluca Romani, Daniele Ragni, Francesco Avallone, and Damiano Casalino. Aeroacoustic investigation of a propeller operating at low reynolds numbers. *AIAA Journal*, pages 1–12, 2021.

[8] Brenda S. Henderson and Dennis Huff. Electric motor noise for small quadcopters: Part ii - source characteristics and predictions. In *2018 AIAA/CEAS Aeroacoustics Conference*, 2018.

[9] Dennis L. Huff and Brenda S. Henderson. Electric motor noise for small quadcopters: Part 1 – acoustic measurements. In *2018 AIAA/CEAS Aeroacoustics Conference*, 2018.

[10] Angus Leslie, Kee Choon Wong, and Doug Auld. Experimental analysis of the radiated noise from a small propeller. In *Proceedings of 20th International Congress on Acoustics, ICA*, 2010.

[11] J. F. Marchman and A. Abtahi. Aerodynamics of an aspect ratio 8 wing at low reynolds numbers. *Journal of Aircraft*, 22(7):628–634, 1985.

[12] Roberto Merino-Martinez, Alejandro Rubio Carpio, Lourenco Lima Pereira, Steve Herk, Francesco Avallone, Daniele Ragni, and Marios Kotsonis. Aeroacoustic design and characterization of the 3d-printed, open-jet, anechoic wind tunnel of delft university of technology. *Applied Acoustics*, 170:107504, 12 2020.

[13] Robert W. Paterson, Paul G. Vogt, Martin R. Fink, and C. Lee Munch. Vortex noise of isolated airfoils. *Journal of Aircraft*, 10(5):296–302, 1973.

[14] Stefan Pröbsting and S. Yarusevych. Laminar separation bubble development on an airfoil emitting tonal noise. *Journal of Fluid Mechanics*, 780:167–191, 10 2015.

[15] Gianluca Romani, Edoardo Grande, Francesco Avallone, Daniele Ragni, and Damiano Casalino. Performance and noise prediction of low-reynolds number propellers using the lattice-boltzmann method. *Aerospace Science and Technology*, page 107086, 09 2021.

[16] Fulvio Scarano and M.L. Riethmuller. Advances in iterative multigrid piv image processing. *Experiments in Fluids*, 29:S051–S060, 04 2012.

[17] Connor E. Toppings and Serhiy Yarusevych. Structure and dynamics of a laminar separation bubble near a wingtip. *Journal of Fluid Mechanics*, 929:A39, 2021.

[18] Justin Winslow, Hikaru Otsuka, Bharath Govindarajan, and Inderjit Chopra. Basic understanding of airfoil characteristics at low reynolds numbers (104–105). *Journal of Aircraft*, 55:1–12, 12 2017.

[19] Serhiy Yarusevych, Pierre Sullivan, and John Kawall. Coherent structures in an airfoil boundary layer and wake at low reynolds numbers. *Physics of Fluids*, 18:044101, 04 2006.

[20] Serhiy Yarusevych, Pierre Sullivan, and John Kawall. On vortex shedding from an airfoil in low-reynolds-number flows. *Journal of Fluid Mechanics*, 632:245, 01 2010.